



# Effect of calcination temperature on the microstructure and electronic properties of TiO<sub>2</sub>–ZnO nanocomposites and implications on photocatalytic activity

N. Gayathri Menon<sup>1</sup> · Sankara Sarma V. Tatiparti<sup>1,2</sup> · Suparna Mukherji<sup>1,3</sup> 

Received: 27 December 2017 / Accepted: 17 April 2018 / Published online: 25 April 2018  
© Springer-Verlag GmbH Germany, part of Springer Nature 2018

## Abstract

TiO<sub>2</sub>–ZnO nanocomposites with a constant Ti:Zn molar ratio of 1:0.1 were prepared via sol–gel process followed by calcination at 300, 400, 500, 600, and 700 °C. The structural and compositional characterizations of these nanocomposites were performed through XRD, FTIR, SEM, and EDAX. Bandgap was measured using DRS. Photocatalytic performance of the nanocomposites was evaluated by decolorization of methyl orange dye under UV and visible irradiation with and without aeration. The results showed that increase in calcination temperature resulted in nanocomposites with well-defined morphology. Although the particle size increased with increase in calcination temperature, the crystallinity of the particles also increased, resulting in enhanced photocatalytic activity. A temperature-dependent anatase-to-rutile phase transformation was observed in TiO<sub>2</sub>–ZnO nanocomposite beyond 600 °C. The calcination temperature influenced both dye adsorption on the nanocomposites and also dye decolorization by photocatalysis. Even when present at low molar concentration, ZnO in the nanocomposite caused sufficient decrease in bandgap (2.6 eV) at temperatures as low as 400 °C, such that visible irradiation could cause dye decolorization. However, the best decolorization performance was observed in the presence of the nanocomposite calcined at 600 °C. Aerated systems showed better performance in all cases. Desorption of the dye remaining adsorbed on the nanocomposite at the end of the photocatalytic reaction, confirmed that adsorption accounted for only 6.6 and 3% of dye removal in the nanocomposites calcined at 600 °C with UV and visible irradiation, respectively. However, in other systems, ignoring adsorption may cause significant overestimation in photocatalytic loss of dye from the system.

**Keywords** TiO<sub>2</sub>–ZnO nanocomposite · Photodecolorization · Methyl orange dye · Calcination temperature · Visible irradiation

**Electronic supplementary material** The online version of this article (<https://doi.org/10.1007/s13204-018-0783-z>) contains supplementary material, which is available to authorized users.

✉ Suparna Mukherji  
mitras@iitb.ac.in

- <sup>1</sup> Centre for Research in Nanotechnology and Science, Indian Institute of Technology Bombay, Mumbai, India
- <sup>2</sup> Department of Energy Science and Engineering, Indian Institute of Technology Bombay, Mumbai, India
- <sup>3</sup> Centre for Environmental Science and Engineering, Indian Institute of Technology Bombay, Powai, Mumbai 400076, India

## Introduction

Heterogeneous photocatalysis, with a primary focus on TiO<sub>2</sub> nanoparticles, has been widely applied for water purification (Das et al. 2014; Liang et al. 2013; Araña et al. 2010; Rizzo et al. 2009 and; Méndez-Arriaga et al. 2008) and disinfection processes (Rodríguez-Méndez et al. 2017; Cai et al. 2014; Tsuang et al. 2008). The photocatalytic property of TiO<sub>2</sub> is attributed to the generation of holes and electrons upon photoactivation (Schneider et al. 2014). TiO<sub>2</sub> exists in three main phases viz. anatase, brookite, and rutile. Rutile is stable, while anatase and brookite are metastable at ambient pressures and temperatures (De Angelis et al. 2014). However, isolation of the brookite phase is difficult, and hence, it is not widely used for photocatalytic applications (Zhang et al. 2014). The energy bandgaps of rutile and anatase are 3.02 and 3.23 eV, respectively (Bojinova et al. 2007; Wang

et al. 2013). High degree of recombination of photogenerated electrons and holes is a major limiting factor controlling its photocatalytic efficiency. This limitation impedes its application for degradation of contaminants in water and air (Devi and Kavitha 2013; Mo and Ching 1995). Thus, a major challenge in heterogeneous photocatalysis using  $\text{TiO}_2$  nanoparticles is the need to facilitate the use of visible light for generation of electrons and holes (Pelaez et al. 2012). Coupled semiconductor photocatalysts are gaining popularity as they are able to achieve more efficient charge separation, increased lifetime of the charge carriers, and enhanced interfacial charge transfer to adsorbed substrates (Janitabar-DarziAli and Mahjoub 2009; Shahram et al. 2016). ZnO has been chosen for the current study as it has a larger band-gap than  $\text{TiO}_2$  and, hence, would be instrumental in efficient charge separation and extending the excitation range of the nanocomposite (Pei and Leung 2013). In this regard, coupling with zinc oxide (ZnO) is advantageous due to its non-toxic nature and low cost. The  $\text{TiO}_2$ -ZnO system has been reported to show enhanced photodegradation efficiency (Cheng et al. 2014; Wang et al. 2013).

The main attributes of a nanocomposite which determine its photocatalytic activity are morphology, crystallinity, crystallite size, and phases present (Bojinova et al. 2007). These attributes may get affected while doping  $\text{TiO}_2$  with ZnO. Liao et al. (2008) showed that both Zn concentration in the system and the surfactant used can affect the various attributes of the nanocomposites, such as photocatalytic activity, morphology, and particle size distribution. The addition of dopants such as Zn in  $\text{TiO}_2$  nanoparticles can significantly affect its photocatalytic activity by altering its electrochemical and optical attributes, such as, band-gap, recombination of electron-hole pairs, and visible light activity (Liao et al. 2008; Rajbongshi et al. 2015; Athauda et al. 2012). The addition of surfactants during synthesis can affect both the electrochemical and optical properties of nanocomposites and nanoparticles in general (Jing et al. 2014). In addition, certain surfactants, due to their branched structure and chemical bonding to the precursor or the nanocrystal formed, can determine the shape and size of the nanoparticles and/or nanocomposites (Liao et al. 2008; Mozafarri et al. 2017). For instance, the addition of surfactants can help in oriented attachment and directed growth of nanocrystals, which can help in manipulation of shape and/or size control. Mozafarri et al. (2017), on the other hand, found that surfactant or capping agents can also control the shape and size of the nanoparticles by associating or binding with both precursor and nanocrystal surface, thereby controlling both nucleation and growth. These properties of nanocomposites may further be tuned by choosing appropriate synthesis conditions. Calcination temperature is one of the most important synthesis conditions that determines the various characteristics of photocatalysts (Wang et al. 2013;

Yu and Wang 2010). Earlier studies were conducted at relatively higher calcination temperatures of 600 °C and above at various Zn concentration. Wang et al. (2013) showed that the calcination temperature and duration played an important role in determining the various phases and the crystallinity of the nanocomposite. However, since a high Zn:Ti molar ratio of 1:1 was used for the synthesis, additional N-doping had to be employed to suppress formation of zinc titanates. The current study explored the effect of calcination temperature in determining these attributes when  $\text{TiO}_2$ -ZnO nanocomposites were synthesized via a previously reported route (Liao et al. 2008). The Ti:Zn molar ratio was kept constant at a lower value as compared to those reported in the literature (1:0.1) and the calcination temperature was varied between 300 and 700 °C to study its effect on microstructure and photocatalytic activity under UV and visible irradiation. The main aim of the present study was to deduce if visible light activity, and hence, enhanced photocatalytic activity could be achieved at lower Ti:Zn ratios and lower calcination temperatures. Aeration is one of the critical operational parameter that can affect the photocatalytic efficiency of nanocomposites (Nguyen et al. 2013; Araña et al. 2010; Fox and Dulay 1993). By comparing air, pure oxygen, and nitrogen purging, Nguyen et al. (2013) showed that air and oxygen purging had a beneficial effect on the production of hydroxyl radicals necessary for the degradation of target compounds during photocatalysis. Oxygen purging facilitates in suppressing the electron hole recombination effect as it acts as an efficient conduction band “electron-trap” (Fox and Dulay 1993). This electron, trapped by oxygen in the air, is essential for generating superoxide radical, which can further increase photocatalytic degradation efficiency by mediating reactions in the bulk (Nishio et al. 2006; Fox and Dulay 1993). While pure oxygen may render better efficiency, purging air is employed more commonly as it is more cost effective. Moreover, aeration may also improve mixing in the system (Araña et al. 2010).

In this paper, the role of the photocatalytic process on decolorization was examined along with sorption of the dye molecules on the photocatalyst. This aspect is important as there is still a lot of debate as to whether photocatalysis is truly a surface mediated reaction or a combination of surface and bulk mediated reactions (Odling and Robertson 2015; Minero et al. 1992). In most publications, the extent of photocatalytic removal is quantified as the cumulative effect of adsorption of the target pollutant and the redox reaction, both of which occur on the surface of the photocatalyst. If this hypothesis is true, then the photocatalytic efficiency would depend on the initial adsorption on the photocatalyst. Another aspect that is often overlooked is that this would lead to overestimation of the amount of the pollutant that is actually removed through photocatalytic degradation. Some of the pollutant may remain adsorbed even after the reaction

is completed. This aspect of photocatalysis needs to be evaluated further. In addition to probing the effects of calcination temperature on the microstructure of the nanocomposite, attempts were also made to quantify the residual pollutant associated with the photocatalyst at the end of the process so as to obtain more accurate estimates on decolorization efficiency due to photocatalysis.

## Materials and methods

### Materials

Reagent-grade Titanium (IV) isopropoxide ( $C_{12}H_{28}O_4Ti$ , TIP) and zinc nitrate hexahydrate ( $Zn(NO_3)_2 \cdot 6H_2O$ , ZN), respectively, were chosen as the Ti and Zn precursors. Ethanol (EtOH) (>98% pure), the surfactant sodium dodecyl sulphate (SDS), and methyl orange dye used in decolorization experiments were obtained from Sigma Aldrich. Reagent-grade HCl,  $HNO_3$ , and HF were obtained from Merck. Distilled (DI) water was used in all experiments and synthesis procedures.

### Synthesis of the $TiO_2$ –ZnO nanocomposites

A simple non-aqueous sol–gel process reported by Liao et al. (2008) was used for synthesis of the nanocomposites. Briefly, a transparent  $TiO_2$  solution was prepared initially by adding the Ti precursor, TIP, dropwise into ethanol under vigorous stirring, so as to attain a TIP:EtOH molar ratio of 1:10. The pH of the solution was adjusted to 2 with HCl. The surfactant, SDS, was then introduced into the system, such that TIP:SDS molar ratio was 1:0.02. For the synthesis of  $TiO_2$ –ZnO nanocomposites, an aqueous solution of ZN (1 mol/L) was added to the  $TiO_2$  solution to achieve ZN:TIP molar ratio of 0.1:1, after the addition of SDS. A mixture of ethanol and distilled water was separately prepared and the above solution was added dropwise into the ethanol–water mixture under constant stirring so as to achieve a molar ratio of 1:4:10 for TIP:H<sub>2</sub>O:EtOH. This solution was kept under static condition to facilitate gelation overnight. The gel was dried at 70 °C to yield yellow crystals which were subsequently powdered with a mortar and pestle and calcined for 1 h. To study the effect of calcination temperature on the microstructure and properties of the nanocomposite, calcination was performed at 300, 400, 500, 600, and 700 °C. The powder obtained after calcination was washed by centrifugation initially with EtOH and later with distilled water, until the supernatant attained a neutral pH. A set of  $TiO_2$  nanoparticles (without any Zn addition) calcined over the same temperature range were also prepared to serve as controls.

### Characterization of the nanocomposites

Field Emission Gun–Scanning Electron Microscopy (FEG–SEM) (JSM 7600F, JEOL, Japan) was used to study the morphology of the particles. Furthermore, the FEG–SEM images were analyzed using ImageJ 1.410 for determination of particle size and aspect ratio of the various samples. Particle size distribution was derived from histograms considering more than 300 particles measured using multiple SEM micrographs. Powder XRD (Philips X'pert PRO, The Netherlands) with Cu- $\alpha$  radiation (1.54 Å) revealed the various phases present. The weight % of anatase and rutile phase was estimated by Spurr–Myers equations (Eqs. 1, 2) (Spurr and Myers 1957):

$$X_A = \frac{100}{(1 + 1.265I_R/I_A)} \quad (1)$$

$$X_R = \frac{100}{(1 + 0.8I_A/I_R)} \quad (2)$$

where  $I_A$  is anatase phase intensity at  $2\theta = 25.25^\circ$  and  $I_R$  is intensity of rutile peak at  $2\theta = 27.7^\circ$ , and  $X_R$  and  $X_A$  are weight percentages of anatase and rutile in the sample, respectively. The various bonds and their frequencies were studied using Fourier Transform Infrared Spectroscopy (FTIR) (Vertex 80 FTIR, Bruker, Germany) in the frequency range of 400–4000  $cm^{-1}$ . Diffuse reflectance absorption spectra (DRS) of the samples were recorded using a spectrometer (3600F, Shimadzu, Japan) equipped with an integrating sphere assembly. From the DRS spectra of the nanocomposites, the transformed reflectance ( $K$ ) as defined by the Kubelka–Munk function (Eq. 3) was obtained from the % reflectance ( $R$ ) values (Yakuphanoglu et al. 2007; Derikvandi and Nezamzadeh-Ejehieh 2017):

$$K = \frac{(1 - R)^2}{2R} \quad (3)$$

The Tauc plots of  $(\alpha h\nu)^n$  versus  $h\nu$  ( $\alpha$ : absorption coefficient,  $\alpha = K$ , when the effect of scattering is assumed to be negligible) were plotted for calculation of bandgap of the nanocomposites. The “ $n$ ” value was taken as  $\frac{1}{2}$  for the  $TiO_2$ –ZnO nanocomposites (indirect bandgap) and 2 for direct bandgap ( $TiO_2$  nanoparticles) (Derikvandi and Nezamzadeh-Ejehieh 2017; Little and Kordesch 2001).

### Estimation of photocatalytic activity

Photocatalytic activity was estimated through the extent of decolorization of the anionic methyl orange (MO) dye solution in the presence of UV and visible light sources of 125 W. MO depicts absorbance maxima at 465 nm.

Decolorization in the presence of a photocatalyst was estimated as decrease in intensity at 465 nm. The reactions were carried out in a custom-made quartz reactor system equipped with a reaction vessel of 200 mL working volume in which the contents were stirred using a magnetic stirrer. The photocatalyst (5 g/L) was added to the reaction vessel containing MO solution (10 mg/L) and stirred in the dark until adsorption–desorption equilibrium was attained. Adsorption kinetics was studied by measuring concentration of dye over time after the nanocomposite was added to the dye solution. Adsorption equilibrium is reached when no further change in dye concentration is observed over time. Subsequently, the light was turned on and samples were taken out intermittently up to 240 min. The photocatalyst was separated by centrifugation at high speed and absorbance at 465 nm was recorded. The normalized dye residual was expressed as  $C/C_0$ , where  $C$  and  $C_0$  denote the dye concentration at any time ( $t$ ) and the initial dye concentration, respectively. Both  $\text{TiO}_2$ –ZnO nanocomposites and  $\text{TiO}_2$  nanoparticles prepared without Zn were used for the decolorization experiments. When samples were extracted at intermediate timepoints, pH was adjusted to 7 with 0.1 M NaOH, since absorption spectra of MO are a function of pH. The  $C/C_0$  profiles were plotted with respect to time. The effect of aeration (at a flow-rate of 3.3 L/min) on both adsorption and photocatalysis was also evaluated by purging air through the system.

In addition, residual dye adsorbed on the nanocomposites and nanoparticles was quantified to evaluate the real amount of dye that was photocatalytically removed from the system and a simple mass balance was performed at the end of the photocatalytic reaction to distinguish between residual dye adsorption and decolorization by photocatalysis. This was done by collecting the particles after the end of the photocatalysis study at 240 min by filtration through a 0.2  $\mu\text{m}$  membrane filter. The absorbance of this solution was used to quantify the mass of dye remaining in the aqueous phase after the reaction had been carried out for the stipulated time of 240 min. Furthermore, the collected particles were resuspended in 10 mL distilled water and centrifuged at 10,000 rpm for 10 min. The absorbance of the supernatant at 465 nm was noted. The pellet was then collected and dried overnight at 105 °C. Weight of the dried pellet was noted. This was then dispersed in 10 mL distilled water and stirred for 30 min, the absorbance at 465 nm was noted, and the weight of the particles were recorded at each step. These steps were repeated thrice to desorb most of the dye adsorbed onto the particles. Cumulative mass quantified during each step of desorption represents the mass of dye that remained adsorbed onto the nanocomposite/nanoparticle after 240 min. The mass of dye remaining in the solution and the mass of dye recovered via desorption from the catalyst helped achieve realistic estimates for photodecolorization. This was compared to the apparent value of the mass lost

during the entire reaction. Recovery efficiency was determined by repeating the experiment for recovery of adsorbed dye soon after adsorption equilibrium was achieved over 90 min in the dark. These studies free of interference from photocatalytic decolorization could provide estimates of recovery efficiency for the protocol discussed above. These experiments were conducted in stirred and aerated systems. All experiments were conducted in duplicate.

## Results and discussion

### Synthesis and characterization of the nanocomposites

The morphology of nanocomposites synthesized via the non-aqueous sol–gel process was studied using FEG–SEM imaging (Fig. 1). The size distribution of the particles, plotted using the ImageJ 1.41O software, is shown in Fig. 2. At lower calcination temperatures of 300 and 400 °C, the particles were agglomerated and the particle size and aspect ratios were determined for agglomerates (considering each agglomerate as single particle) rather than for individual particles. This was done, because the individual particles were difficult to distinguish and mark in the software. For particles calcined at 500 °C and above, the particle boundaries were distinct, and hence, particle diameters and aspect ratios could be determined. Highly clustered and agglomerated fine particles were observed at the lower calcination temperatures of 300 and 400 °C. At such lower calcination temperatures, the supplied thermal energy was not sufficient to cleave the agglomerates into finer entities. Therefore, at lower temperatures, agglomeration is predominant (Fig. 1a, b). The particle sizes increased with an increase in calcination temperature from 300 to 600 °C. At temperatures 500 and 600 °C, the particles were well-defined, smooth-surfaced, and nearly cubical in morphology with mean aspect ratio close to 1 (Fig. 2c, d). At calcination temperature of 700 °C, a slight change in the particle morphology was observed (Fig. 2e) compared to that at 500 and 600 °C. This attribute was also visible in the bimodal particle size distribution shown in Fig. 2e, a dual mean aspect ratio of  $0.9 \pm 0.3$  (cubical particles or equiaxed morphology) and  $1.4 \pm 0.1$  (elongated stacked morphology). At higher calcination temperatures, the agglomerates cleave into smaller versions and/or individual particles. These particles possessed higher surface energy resulting from their larger surface area (and curvature). Thus, they grew in size to decrease the surface energy and surface curvature. The presence of smaller versions of agglomerates and/or individual particles was evident from the reduced seam around the agglomerates/particles at higher calcination temperatures (Fig. 1c–e).

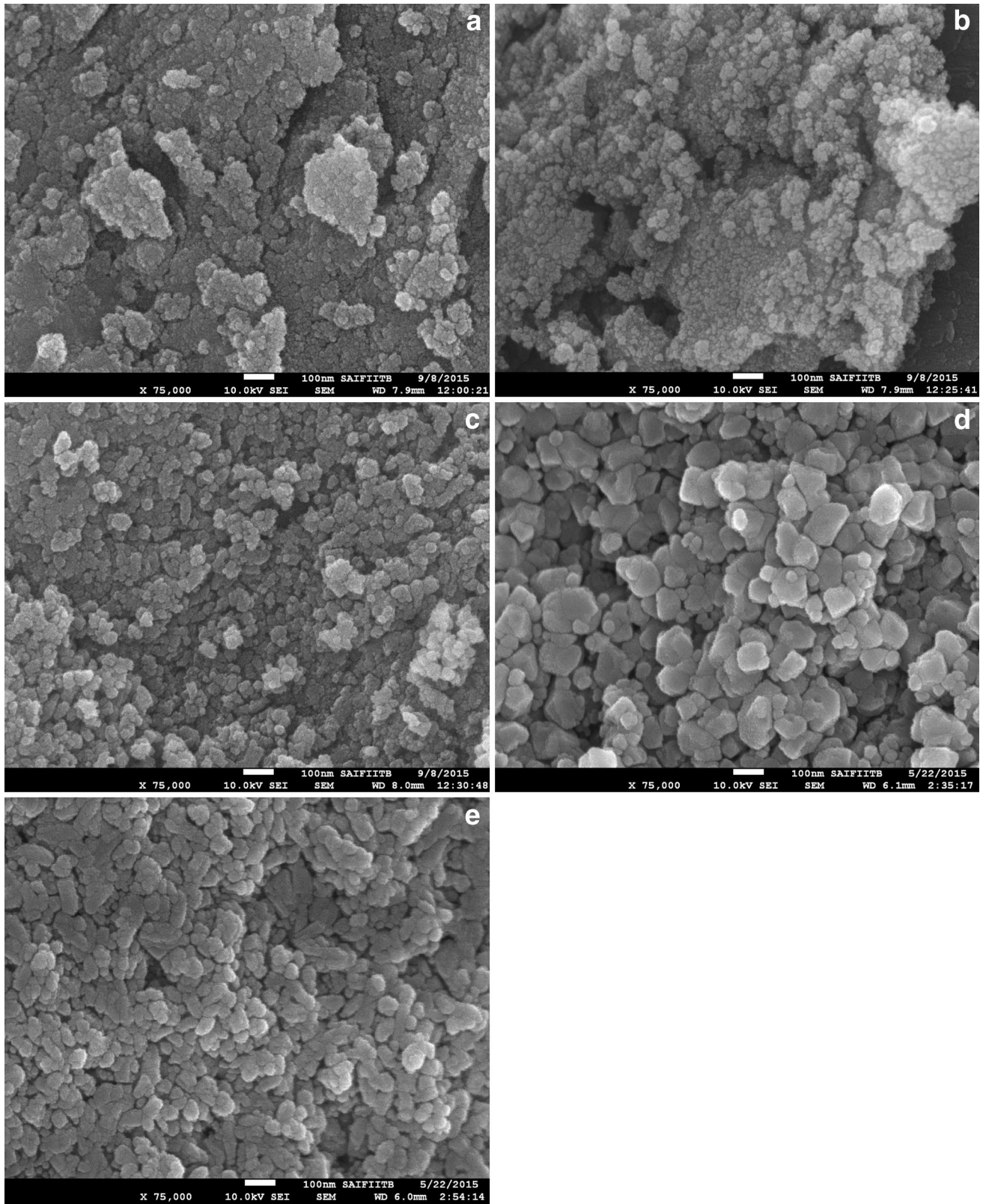
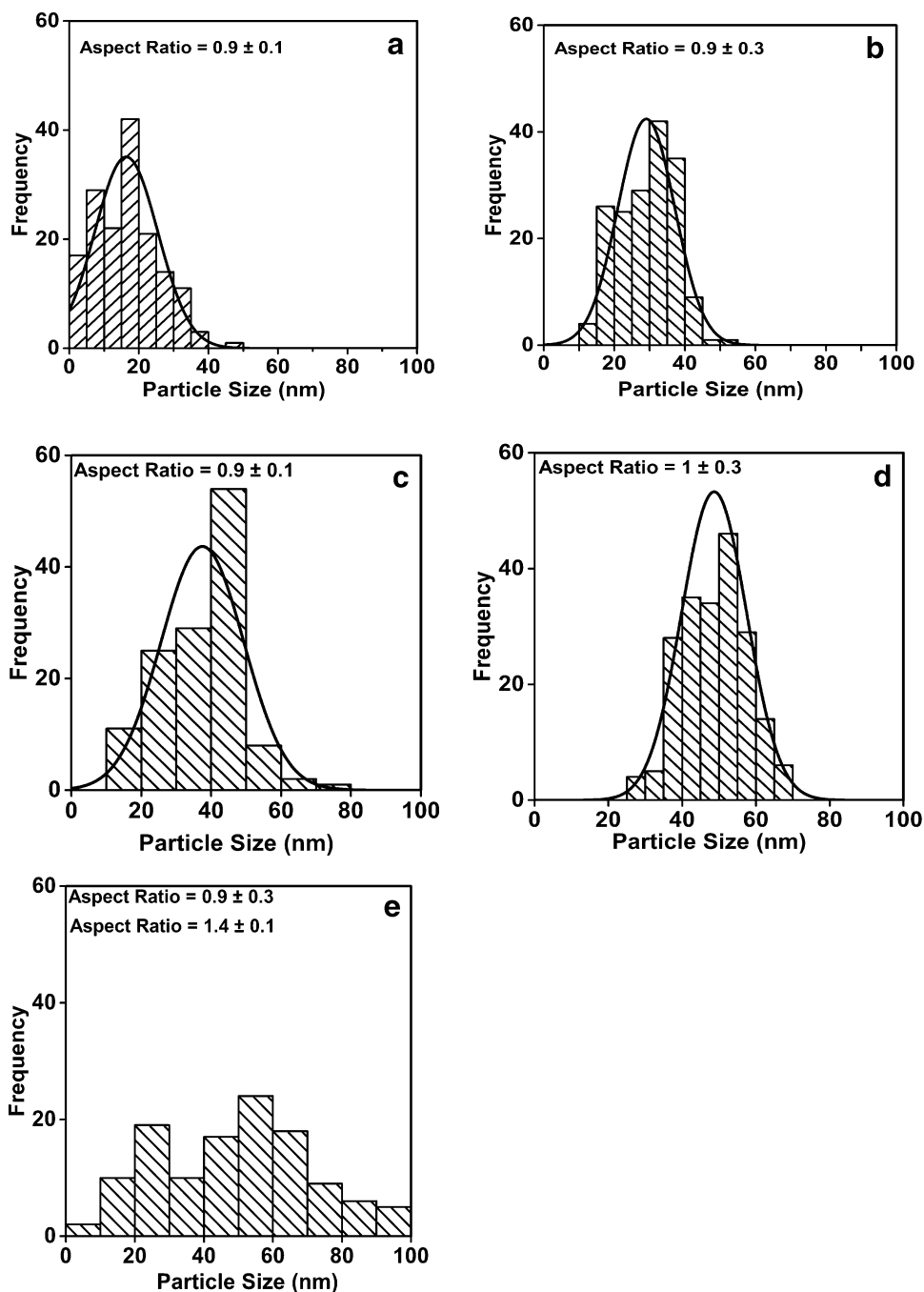


**Fig. 1** FEG–SEM images of nanocomposites calcined at **a** 300 °C, **b** 400 °C, **c** 500 °C, **d** 600 °C, and **e** 700 °C

**Fig. 2** Particle size distribution of nanocomposites calcined at **a** 300 °C, **b** 400 °C, **c** 500 °C, **d** 600 °C, and **e** 700 °C



The various phases in the nanocomposites were analyzed using XRD. The XRD profiles, the major phases present, and their corresponding Miller indices for all the samples are shown in Fig. 3. With increase in calcination temperature from 300 to 700 °C, increase in crystallinity was observed from the XRD results. Zhang et al. (2000) suggested that the transformation of  $\text{TiO}_2$  from amorphous to anatase was complete beyond 450 °C. This was in consensus with the observations in the current study, wherein the crystallinity of the particles increased significantly at 500 °C and above

as is evident from the increased sharpness of the diffraction peaks. Another interesting observation was that only anatase phase (JPCDS 21-1272) of  $\text{TiO}_2$  was present in particles calcined at temperatures up to 600 °C (denoted by A in Fig. 3). Peaks at 2-theta values  $25.3^\circ$  (0 1 1),  $38.02^\circ$  (0 0 4),  $48.01^\circ$  (0 2 0),  $53.87^\circ$  (0 1 5),  $55.33^\circ$  (1 2 1),  $63.06^\circ$  (0 2 4),  $68.91^\circ$  (1 1 6),  $69.98^\circ$  (2 2 0), and  $75.38^\circ$  (0 3 1) corresponded well with the anatase phase of  $\text{TiO}_2$  (Fig. 3). Peaks for ZnO were not visible in XRD (Fig. 3), since its mass fraction in the nanocomposite was low (Ti:Zn = 1:0.1). Hence, for ZnO,

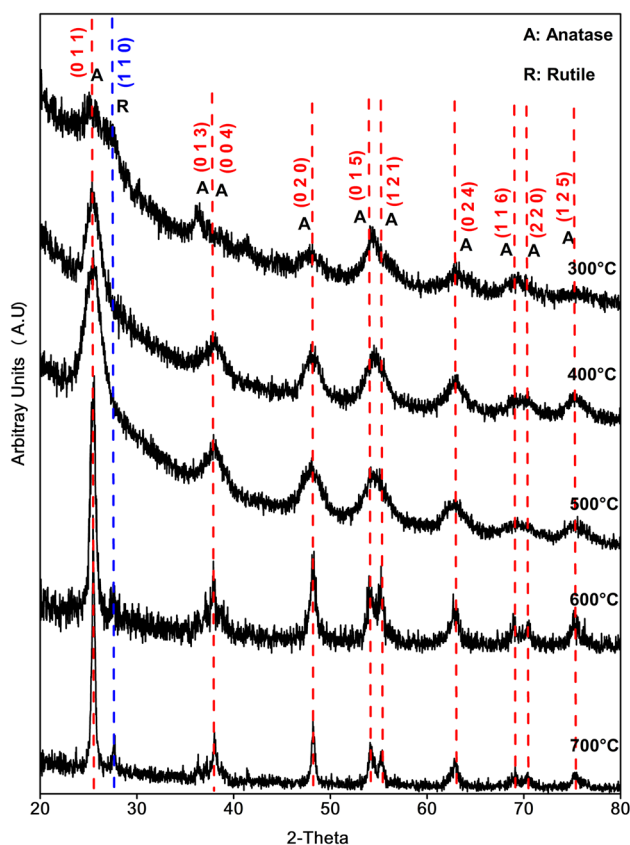


**Fig. 3** XRD pattern of the nanocomposites calcined at various temperature. Miller indices of the various anatase (A) and rutile (R) peaks are shown in red and blue text, respectively

the Miller indices cannot be determined. However, zinc was present in the nanocomposites as is evident from the EDAX spectra, where peaks corresponding to Zn were observed at 1, 8.6, and 9.7 keV (Online resource, ESM 1). Moreover, when the synthesized nanocomposites (after several washing steps) were subjected to microwave digestion using aqua regia and HF and the filtered solution was analyzed in ICP-AES, the presence of Zn in the nanocomposite was confirmed (Online resource, ESM 2). Calculated values of Zn/Ti in the system varied from 0.14 to 0.16 when nanocomposites were synthesized using Zn/Ti design value of 0.1 (ESM 2). At higher Zn:Ti design ratios of 0.2 and above, the presence of zinc oxide was confirmed in the XRD and the miller indices were determined as (0 1 0), (0 1 1), (0 1 2), and (0 1 3) (unpublished results). The presence of anatase is beneficial, since it is reported to be the most photocatalytically active phase of TiO<sub>2</sub> (Luttrell et al. 2014). However, at 700 °C calcination temperature, a small rutile peak was formed at 27.7° (1 1 0) due to phase transformation from anatase to rutile (Fig. 3, JCPDS 76–1940). Phase transformation from anatase to rutile is widely reported in the literature (Yu and Wang 2010, Su et al. 2008). However, in TiO<sub>2</sub> alone, such

a phase transformation was reported at temperature beyond 550 °C based on XRD spectra (Araña et al. 2010; Yu and Wang 2010, Su et al. 2008; Zhang et al. 2000; Gallardo et al. 1995). The phase transformation was attributed to the metastable nature of anatase at high temperature (> 550 °C) and particle size greater than 32–42 nm (Li et al. 2005). It has been reported that rutile particles grow in size at the expense of anatase particles (Li et al. 2005). In the current study, the presence of both anatase and rutile at 700 °C (but not at 600 °C and lower temperatures) was evident from the XRD spectra and also from FEG–SEM images that revealed bimodal particle size distribution only at 700 °C calcination temperature (Figs. 1e, 2e). However, studies by Gribb and Banfield (1997) showed that in pure TiO<sub>2</sub> nanoparticles synthesized by sol–gel or hydrothermal routes using TIP as precursor, anatase-to-rutile phase transformation commenced at particle sizes > 10 nm and calcination temperature > 525 °C. In the present study, although similar synthesis conditions were adopted, the anatase-to-rutile phase transformation was initiated at a higher calcination temperature (> 600 °C). The mean particle size at 600 °C where only anatase phase was present was 50 nm (Fig. 2d). The difference observed is possibly due to the presence of zinc, which may have altered the stability of anatase and/or retarded the phase transformation. With increasing calcination temperature from 300 to 700 °C, peak intensities of anatase phase in the XRD spectra steadily increased and the width of XRD diffraction peaks became narrower, indicating the formation of larger TiO<sub>2</sub> crystallites and increased crystallinity (Wang et al. 2013). This observation is in consensus with Çomaklı et al. (2016), who noticed that anatase TiO<sub>2</sub> was stable on Ti plates up to a calcination temperature of 700 °C. The weight percentage of rutile phase in the sample calcined at 700 °C was quantified using the empirical Spurr–Meyers equation. It was seen that the samples calcined at 700 °C contained 83% anatase and 17% rutile TiO<sub>2</sub>, while all other samples consisted solely of anatase TiO<sub>2</sub>. Anatase-to-rutile phase transformation was manifested as clustering in the morphology of the sample calcined at 700 °C (Fig. 1e) and the corresponding bimodal distribution in the particle size (Fig. 2e).

The bond frequencies of various bonds in the samples are recorded using FTIR spectroscopy and are shown in Fig. 4. In all the spectra, peaks appeared predominantly at three wavenumber ranges: ~3400 and ~1600 cm<sup>-1</sup> in the high-energy range and between 400 and 800 cm<sup>-1</sup> in the low-energy range. The broad peaks at 3346 cm<sup>-1</sup> correspond to OH-stretching vibrations (Athauda et al. 2012). These peaks were due to the presence of moisture in the samples. As the calcination temperature increased, the intensity of these peaks decreased as expected. Peaks observed in the range of 1700–1500 cm<sup>-1</sup> were due to the H–O–H-bending vibrations of physisorbed water. This particular peak was seen to steadily increase in intensity up to the calcination

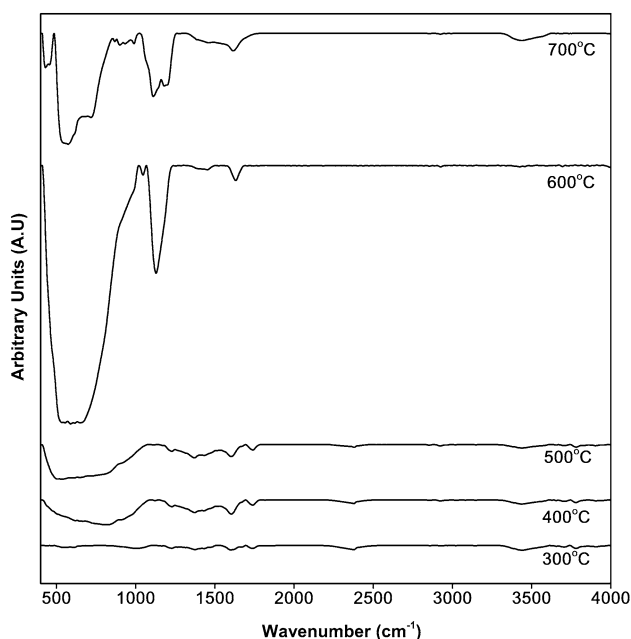


**Fig. 4** FTIR spectra of the nanocomposites calcined at various temperature

temperature of 600 °C and then decrease at 700 °C. The decrease in peak intensity was consistent with the formation of rutile phase (Fig. 3). Amount of water physisorbed on the surface of the catalyst is usually estimated using this peak. Nanoparticles with high specific surface area can adsorb many molecules of water on specific surface active sites and can form  $\text{Ti}^{4+}\text{-OH}_2$  (Choudhury and Choudhury 2013). Therefore, increase in the intensity of this peak may provide an indirect measure of increase in surface area of the catalyst. It is reported that upon increase in calcination temperature beyond 700 °C, the water molecules on the surface attached to  $\text{Ti}^{4+}$  are dissociated. Concomitant formation of new Ti–O bonds facilitates the formation of rutile phase (Choudhury and Choudhury 2013). Thus, intensity of this peak was decreased beyond 600 °C when formation of rutile phase was observed (Fig. 3). In addition, in case of particles calcined at 600 and 700 °C, there were peaks at  $\sim 1200\text{ cm}^{-1}$ . This could be attributed to Ti–O–H-stretching vibrations or remnants of organic species such as C=O or C–O bending vibrations (Cheng et al. 2014).

In the low-energy interval, the stretching vibration band of Ti–O–Ti was observed at approximately  $600\text{ cm}^{-1}$ . The presence of this band indicated the hydrolysis ( $\text{Ti-OR} \rightarrow \text{Ti-OH}$ ) and condensation ( $\text{Ti-OH} + \text{Ti-OR}$  (or  $\text{Ti-OH}$ )  $\rightarrow \text{Ti-O-Ti}$ ) reactions of TIP that is necessary for the formation of  $\text{TiO}_2$  nanoparticles (Athauda et al. 2012). This band was also seen to intensify with increase in calcination temperature. This phenomenon may be attributed to the increased crystallization of  $\text{TiO}_2$  particles at

**Table 1** Bandgaps of the various nanocomposites determined from Tauc plots

Calcination Temperature (°C)	Bandgap (eV)	
	$\text{TiO}_2$	$\text{TiO}_2/\text{ZnO}$
300	2.9	2.9
400	2.8	2.6
500	3.0	2.7
600	3.2	2.8
700	3.2	2.7

higher calcination temperatures. The band at  $440\text{ cm}^{-1}$  is attributed to the Zn–O vibration (Athauda et al. 2012). This band was clearly visible only in samples calcined at 600 °C and above, although a slight shoulder is visible in the sample calcined at 500 °C. It was also observed that the band at  $600\text{ cm}^{-1}$  broadened with increase in calcination temperature. Peaks around  $800\text{ cm}^{-1}$  may represent both symmetric stretching vibration of the Ti–O–Ti and vibration mode of Zn–O–Ti groups (Wang et al. 2013). The presence of Zn–O–Ti vibration may, therefore, indicate that ZnO nanoparticles are present in close proximity to  $\text{TiO}_2$  nanoparticles.

Optical bandgaps were estimated for the various nanocomposites by converting the diffuse reflectance values into the Kubelka–Munk function and then plotting them against the energy value corresponding to the excitation wavelength (Derikvandi and Nezamzadeh-Ejehieh 2017; Yakuphanoglu et al. 2007). Tauc plots for all the samples are given in online resource (ESM 3). The bandgap values obtained from the Tauc plots are summarized in Table 1. It was assumed that the nanocomposite particles would contain mostly indirect bandgaps (hence,  $n = 1/2$ ). At each of the calcination temperature above 300 °C, the bandgap reduced with the addition of Zn in the nanocomposites compared to undoped  $\text{TiO}_2$  nanoparticles with no Zn, although the reduction was only marginal. The minimum bandgap (2.6 eV) was obtained for particles calcined at 400 °C. A possible reason could be due to the relative positioning of the bandgaps of the various phases, i.e., anatase, amorphous  $\text{TiO}_2$ , and ZnO. This may lead to a favorable placement of the various energy levels, which may decrease the effective bandgap of the nanocomposite (Conesa 2012). This effect was seen to be enhanced in particles calcined at 700 °C, where, in addition to anatase  $\text{TiO}_2$  and ZnO, the presence of rutile  $\text{TiO}_2$  was also observed (Fig. 3). Therefore, it can be clearly seen that the addition of Zn in the nanocomposite system had a clear effect on phase crystallization and this in turn also decreased its bandgap. However, it was seen that as the calcination temperature increased, a marginal increase in bandgap was observed. This may be attributed to a decrease in the amorphous content. The sufficiently low bandgap in



the TiO<sub>2</sub>-ZnO nanocomposites may lead to photocatalytic activity under visible light.

### Evaluation of photocatalytic activity

Decolorization of methyl orange (MO) dye (10 mg/L) was studied in the presence of various catalysts (5 g/L) to evaluate the effect of calcination temperature on photocatalysis. MO is an anionic azo dye which is also used as a pH indicator. In acidic and basic media, the color of the dye is red and orange, respectively. The pH was observed to drop spontaneously over the course of the photocatalytic reaction. This change is expected to cause a shift in the absorbance spectra of the dye such that the absorbance maxima would shift due to ionization of the dye. The absorbance at 465 nm may fall simply due to the pH effect (ionization) and not due to transformation of the parent molecule causing decolorization. Thus, decrease in absorbance at 465 nm would not correlate with true color removal. To avoid artifacts due to ionization, pH of the sample drawn was always corrected to 7 using 0.1 M NaOH solution before absorbance was recorded at 465 nm. This protocol has been used by several researchers (Lei et al. 2013; Al-Qaradawi and Salman 2002). Light controls were conducted to rule out the possibility of photolysis of the dye. This was done in the presence of both UV and visible light. The results obtained are depicted in Online Resource (ESM 4). Negligible degradation of the dye was observed in the presence of UV and visible light alone.

It was inferred that dye removal that occurred under dark conditions in presence of the nanocomposite was entirely

due to adsorption. The dye solution was stirred with particles in the dark to attain adsorption–desorption equilibrium, characterized by constant dye concentration. Subsequently, the lamp was switched on after sufficient time was provided for attaining equilibrium. It can be inferred from Fig. 5a, b that the extent of adsorption varied with the calcination temperature of the nanocomposite and aeration. The maximum time required for achieving adsorption equilibrium was determined as 90 min in aerated systems (Fig. 5a). However, in systems without aeration, there was a marked decrease in the extent of dye adsorbed on to the nanocomposites (Fig. 5b). In non-aerated system, the time required to attain equilibrium was found to depend on the calcination temperature of the nanocomposite, as depicted in Fig. 5b. Equilibrium was attained at 60 min for particles calcined at 300 and 500 °C, at 90 min for particles calcined at 400 °C and at 120 min for particles calcined at 600 and 700 °C (Fig. 5b). Figure 5b depicting adsorptive removal of dye in non-aerated system showed a trend with temperature while no clear trend with temperature was observed for aerated system (Fig. 5a). However, it may be noted that both in Fig. 5a, b, adsorption was least at the lowest calcination temperature, intermediate at calcination temperature of 400 and 500 °C and highest at temperatures of 600 and 700 °C. While the maximum extent of adsorption was seen for particles calcined at 600 °C in the aerated system (Fig. 5a), in non-aerated system the particles calcined at 700 °C showed the highest adsorption. The extent of adsorption at 600 and 700 °C was almost comparable in the non-aerated system (Fig. 5b). However, maximum adsorption in systems without

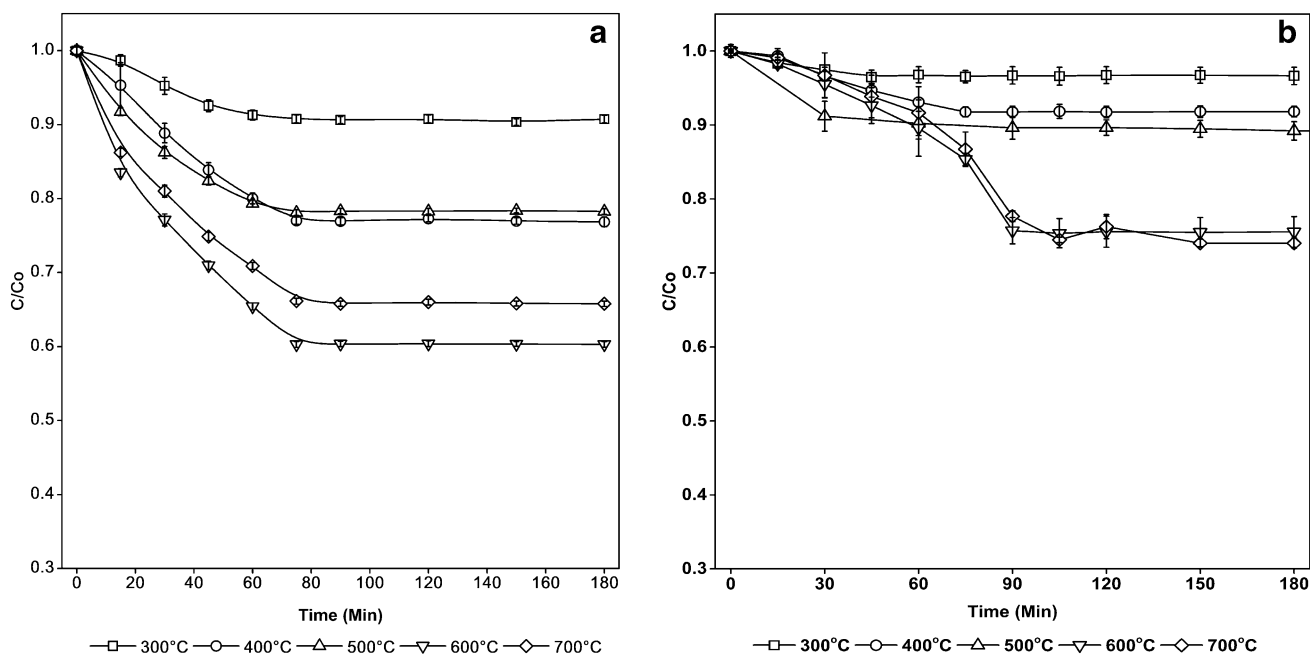
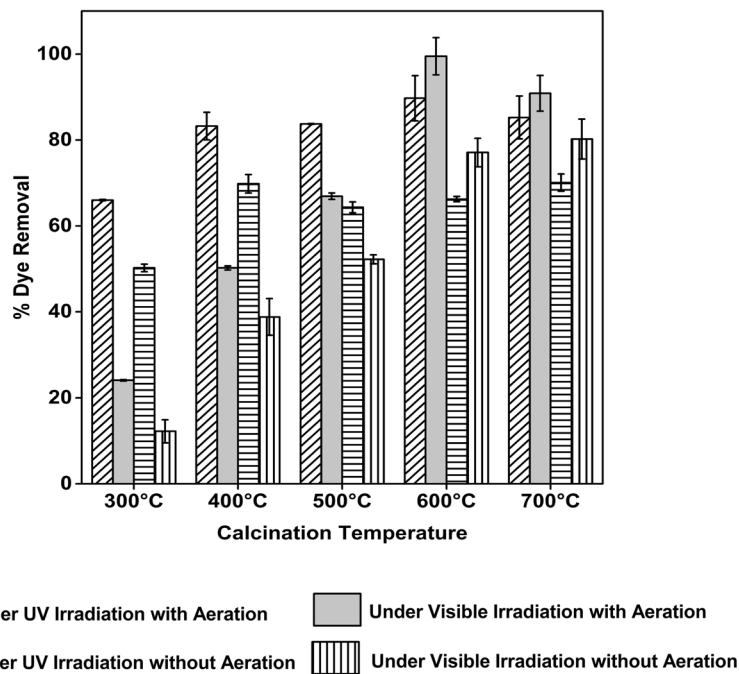


**Fig. 5** Adsorption kinetics of MO dye using nanocomposites calcined at various temperatures in **a** presence and **b** absence of aeration

aeration was significantly lower than in the aerated system. Thus, aeration caused greater rate and extent of dye adsorption possibly by enhancing mixing, preventing agglomeration and settling of particles, reducing boundary layer thickness and increasing film diffusion and enhancing diffusive transport within the particles. Increased crystallinity probably facilitated greater adsorption on nanocomposites calcined at temperature  $\geq 600$  °C compared to those calcined at lower temperature where amorphisity was higher (Fig. 3). Possibly inadequate mixing, agglomeration and rate-limited adsorption may have adversely affected adsorption in non-aerated systems. In aerated systems, adsorption in nanocomposites calcined at 400 and 500 °C was comparable and adsorption on nanocomposite calcined at 600 °C was significantly higher than those calcined at 500 °C and also at 700 °C. Lower adsorption at calcination temperature of 700 °C compared to that at 600 °C in aerated system may be due to phase transformation to rutile that is characterized by larger crystallite size compared to anatase as evidenced from the XRD spectra (Fig. 3). This transformation is expected to decrease the surface area and reduce adsorption. The highest extent of dye removal from aqueous phase by adsorption was  $\sim 45\%$  and this value was observed for the nanocomposite calcined at 600 °C in aerated system. Higher calcination temperatures of 500 °C and above is reported to increase the surface area and porosity of  $\text{TiO}_2\text{-ZnO}$  particles (Liao et al. 2008). This observation was also consistent from the FTIR spectra where the intensity of the peak due to physisorbed water attained maximum value for samples calcined at 600 °C (Fig. 4). This indicates an increase in surface area of the nanocomposites up to a temperature of 600 °C.

**Fig. 6** Extent of decolorization of MO dye after 240 min of exposure to UV and visible irradiation in systems containing  $\text{TiO}_2\text{-ZnO}$  nanocomposites calcined at various temperature in the presence and the absence of aeration



## Photocatalytic decolorization

### Effect of aeration, irradiation source and calcination temperature on extent of decolorization

A comparison of photocatalytic decolorization of MO dye followed by the various nanocomposites under UV and visible irradiation with and without aeration is depicted in Fig. 6. Equal time period of irradiation was given for all systems and the % removal of dye from the aqueous system was computed at the end of 240 min. It was observed that the extent of decolorization reduced markedly when the system was not aerated irrespective of the light source and the calcination temperature of the nanocomposite. This phenomenon may be attributed to two factors. First, aeration greatly improves mixing and its absence may have led to incomplete mixing and hence reduced adsorption and reduced reactivity (Nishio et al. 2006). Second, several authors have postulated the contribution of dissolved oxygen in the air increases the generation of superoxide radicals by electron scavenging from the conduction band (Nishio et al. 2006; Fox and Dulay 1993). Electron scavenging can be beneficial as it suppresses the electron–hole recombination, leading to improved photocatalytic activity.

For UV irradiation with aeration, the extent of removal was almost comparable for the calcination temperature range 400–700 °C. This result is possibly due to the increased energy of electrons generated under UV irradiation. For visible irradiation with aeration, the extent of removal was significantly affected by calcination temperature and removal was highest at 600 °C. The two temperatures that

showed the highest overall removal also showed the highest adsorption (600 and 700 °C) (ESM 3). However, there appears to be no correlation between bandgap lowering and dye removal. Bandgap lowering was much higher at 400 °C than at 600 °C. The results indicate that bandgap lowering in samples calcined at 400 °C is due to presence of amorphous TiO<sub>2</sub>. Amorphousness in these samples is evident from the XRD spectra (Fig. 3). As crystallinity improved with increase in calcination temperature, the bandgap increased (i.e., for samples calcined at 600 and 700 °C) (Table 1, ESM 3), adsorption increased, and photocatalytic activity was also enhanced. However, while samples calcined at 600 °C have a wider bandgap compared to those calcined at 400 °C, its bandgap is lower than that of pure anatase phase TiO<sub>2</sub> (bandgap = 3.2 eV) (Table 1). This effect is due to the presence of Zn in the nanocomposite. Thus, Zn addition coupled with improved crystallinity imparted better photocatalytic activity under visible irradiation.

It was found that in the absence of aeration, the nanocomposite calcined at 600 and 700 °C showed almost comparable extent of decolorization at the end of 240 min under both UV and visible irradiation. In the absence of aeration, the nanocomposite calcined at 700 °C was able to achieve total dye removal of  $70 \pm 3$  and  $80 \pm 5\%$  under UV and visible irradiation, respectively. Under similar conditions, the nanocomposite calcined at 600 °C achieved removal of  $66 \pm 1\%$  under UV irradiation and  $77 \pm 2\%$  under visible irradiation. Thus, in absence of aeration, adsorption and photocatalytic activity were both comparable for the nanocomposites calcined at 600 and 700 °C. For the crystalline nanocomposite calcined at 700 °C containing both rutile and anatase, the increase in adsorption as a result of aeration was relatively lower and increase in photocatalytic removal as a result of aeration was also lower. It was reported that rutile phase is unable to absorb oxygen (Fox and Dulay 1993). Hence, although aeration improved decolorization in all the systems (Fig. 6), the effect of aeration was not as pronounced on the nanocomposite containing rutile phase together with anatase (calcined at 700 °C) in comparison with the other nanocomposites (calcined at 600 °C and lower) comprising solely of the anatase phase (Figs. 5b, 6). The beneficial effect of aeration is possibly due to a combination of improved mixing, improved adsorption, and improved photocatalysis.

#### Effect of calcination temperature on rate and extent of decolorization in aerated system

The pattern of photocatalytic decolorization of MO dye followed by the various nanocomposites under UV and visible irradiation in aerated systems is shown in Fig. 7a, b, respectively. In Fig. 7, time  $t=0$  min indicates time at which the lamp was turned on, after adsorption equilibrium was attained. It was seen that in all cases, irrespective of the

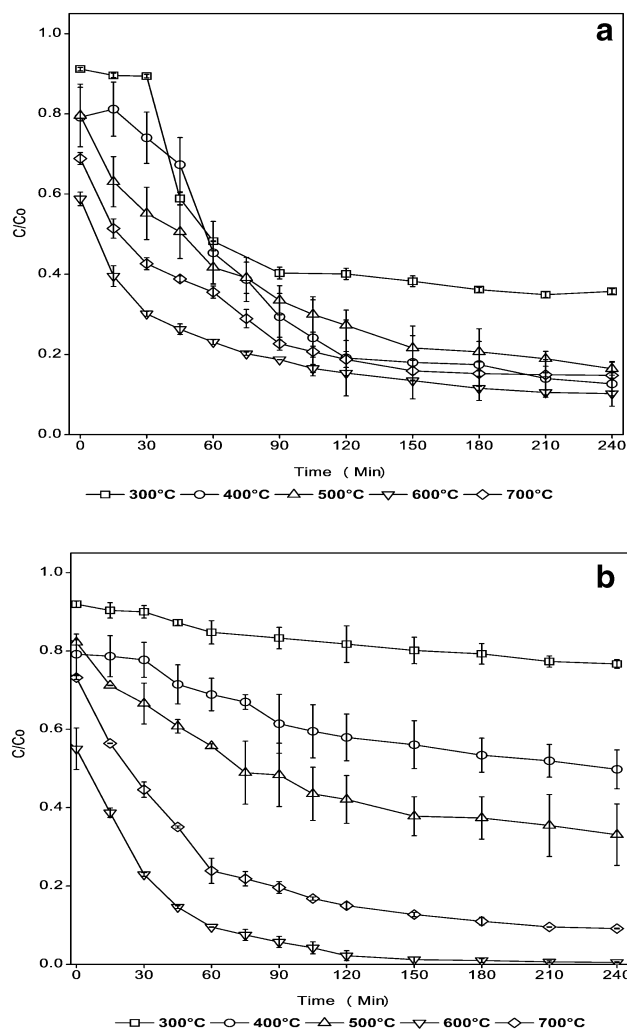


**Fig. 7** Decolorization kinetics of MO dye using the nanocomposites exposed to **a** UV and **b** visible irradiation in aerated systems

calcination temperature, these nanocomposites demonstrated photocatalytic activity under both UV as well as visible irradiation. However, increase in calcination temperature increased the photodecolorization potential significantly. The photocatalytic behavior of the TiO<sub>2</sub>–ZnO nanocomposite powder is reported to be related to the crystallinity, phases present, and particle morphology (Wang et al. 2013). In this study, with increase in calcination temperature from 300 to 600 °C, the crystallinity of the composite powder was seen to increase, as revealed in Fig. 3. Hence, there was an increase in adsorption and photocatalytic decolorization of the dye with increase in calcination temperature from 300 to 600 °C. At all the calcination conditions, the anatase phase of TiO<sub>2</sub>, which is also the most photocatalytically active phase, was present. Thus, the enhanced photocatalytic activity can be attributed to increased crystallinity alone. Interestingly, however, for samples calcined at 700 °C, it was observed that the decolorization attained under both UV

and visible irradiation was close to that achieved for samples calcined at 600 °C. A UV light-induced removal of  $90 \pm 5\%$  and  $85 \pm 5\%$  was attained in case of samples calcined at 600 and 700 °C, respectively. In case of visible light irradiation, the particles calcined at 700 °C showed comparable activity ( $91 \pm 4\%$ ) as compared to samples calcined at 600 °C ( $99 \pm 4\%$ ). Contrary to the current study, Gao et al. (2011) reported that maximum adsorption and photocatalytic decolorization of a dye were attained at a relatively lower temperature of 400 °C. They attributed the decreased adsorption and photocatalysis at higher temperatures to formation of rutile  $\text{TiO}_2$  in the otherwise anatase  $\text{TiO}_2$ -ZnO nanocomposite. In the present study, it was observed that the presence of rutile phase decreased the adsorptive capability of the nanocomposite (Fig. 6); however, high photocatalytic activity was retained. It was observed that visible light activity was retarded for particles calcined at 300 and 400 °C. This may be attributed to the amorphous nature of the samples (Wang et al. 2013).

The decolorization results for each nanocomposite were compared with the activity of  $\text{TiO}_2$  nanoparticles prepared at the corresponding calcination temperature (Fig. 8). Overall removal of the dye from the aqueous phase due to adsorption at 90 min (Fig. 8a) and decolorization after 240 min is depicted in Fig. 8b. At any calcination temperature, the  $\text{TiO}_2$  nanoparticles achieved removal comparable to that of the  $\text{TiO}_2$ -ZnO nanocomposite in the presence of UV light. However, in the presence of visible light, MO removal by

$\text{TiO}_2$  NPs was significantly lower than that of  $\text{TiO}_2$ -ZnO nanocomposite. The removal reported for  $\text{TiO}_2$  NPs calcined at 300 and 400 °C under visible irradiation was almost entirely due to adsorption. However, even at these temperatures, some dye decolorization was observed for the nanocomposite under visible irradiation.

### Evaluation of residual adsorption on nanocomposites

The residual adsorption of the dye on the nanocomposites was quantified after centrifugation followed by three cycles of desorption. Recovery efficiency of dye was computed after adsorption on the nanoparticles/nanocomposites (in the dark) for 90 min (Online resource, ESM 5). Across all the calcination temperatures, a high recovery efficiency of MO adsorbed on  $\text{TiO}_2$ -ZnO nanocomposites and  $\text{TiO}_2$  nanoparticles in the range of  $81 \pm 7$  to  $96 \pm 9$  was observed using the protocol followed. Thus, the error due to incomplete recovery is relatively low and was ignored while estimating mass distribution at the end of photocatalytic reaction. Mass balance of MO dye in the various systems at the end of the photocatalytic reaction using UV and visible irradiation is summarized in Fig. 9 (data provided in Online resource, ESM 6). The observed loss from aqueous solution is a cumulative effect of photodecolorization as well as adsorption on to the catalyst. Thus, apparent loss due to photocatalysis may be overestimated as a result of sorption on the catalyst.

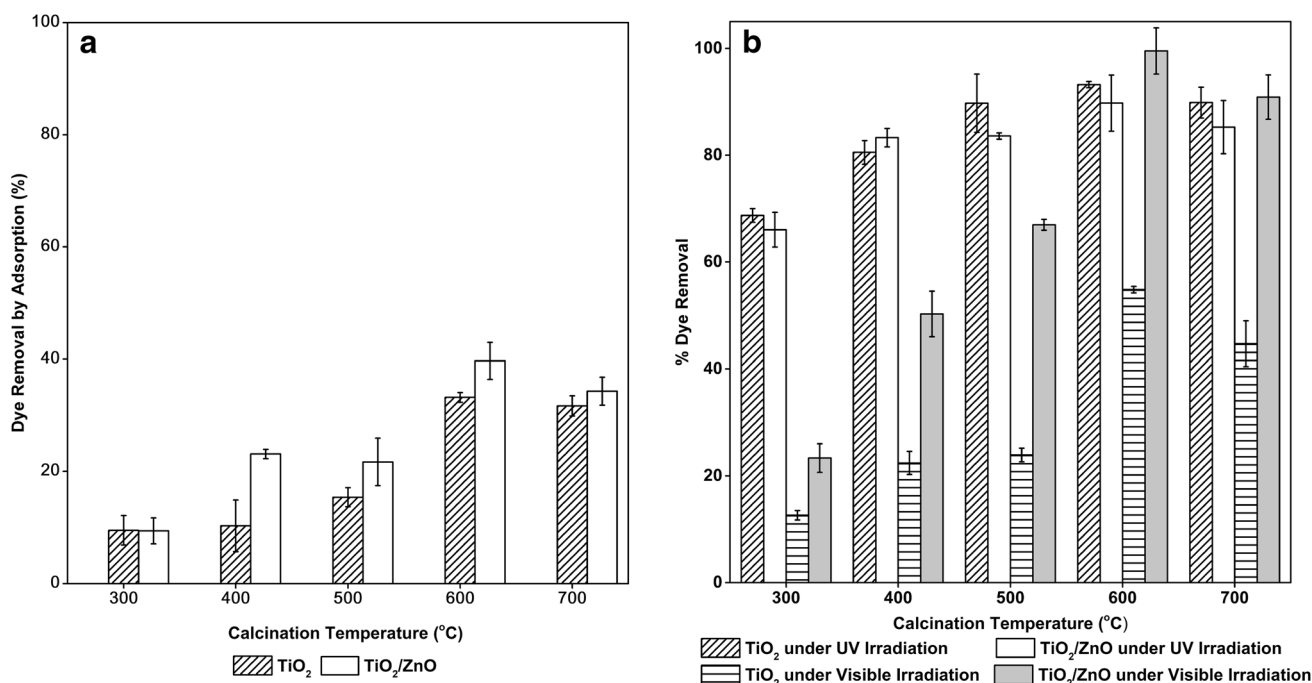


**Fig. 8** Comparison of % dye removal at 240 min by  $\text{TiO}_2$  particles and  $\text{TiO}_2$ -ZnO nanocomposites calcined at various temperatures through **a** adsorption and **b** photocatalysis

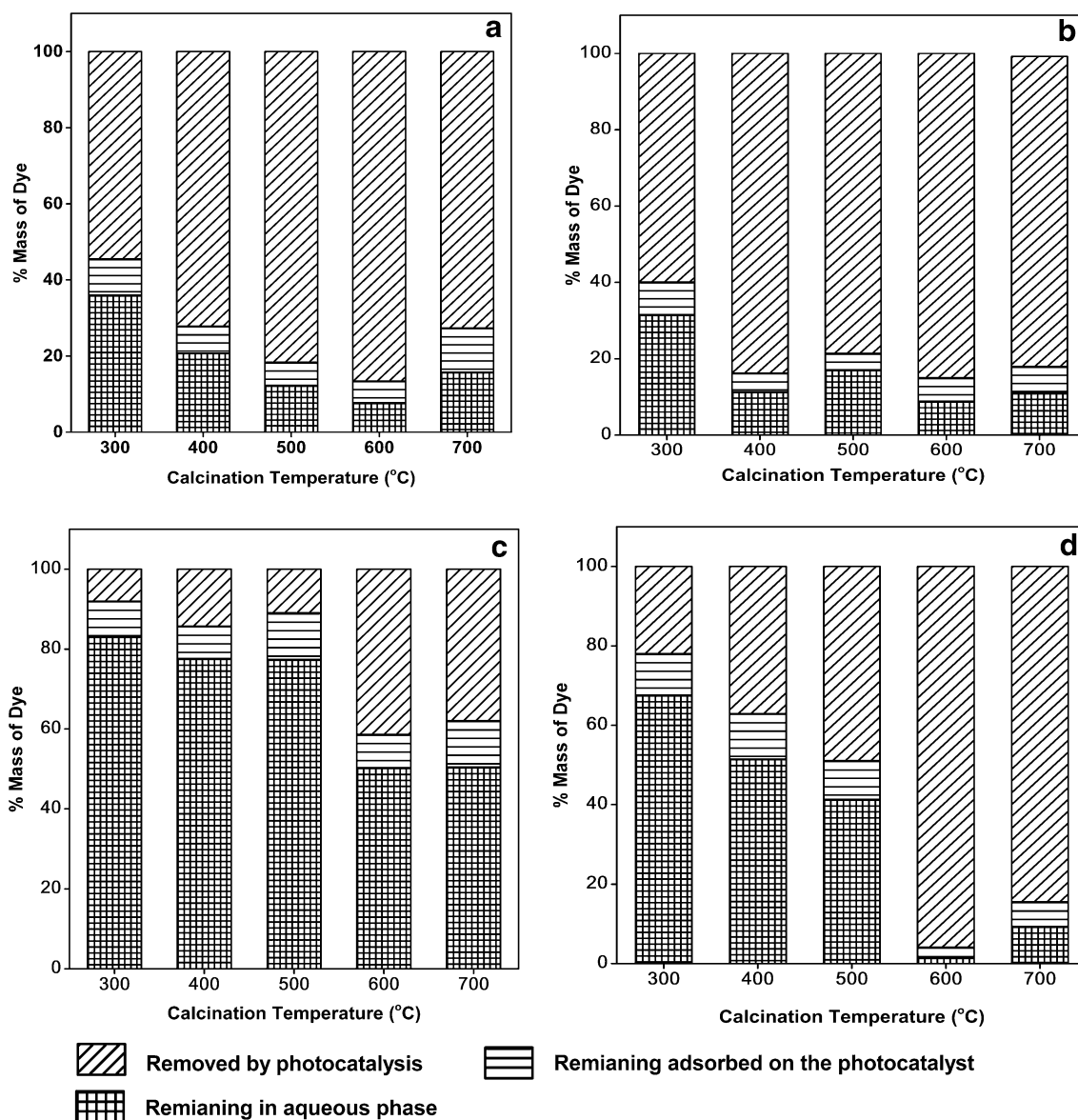


**Fig. 9** Mass balance of MO dye at the end of the photocatalytic reaction in various systems **a** TiO<sub>2</sub>-ZnO nanocomposite under UV irradiation, **b** TiO<sub>2</sub>-ZnO nanocomposite under visible irradiation, **c** TiO<sub>2</sub>

nanoparticles under UV irradiation, and **d** TiO<sub>2</sub> nanoparticles under visible irradiation

Three major observations were made from this study. First, at all calcination temperatures, some amount of dye remained adsorbed on the catalyst even after the reaction was assumed to be complete (indicated by the disappearance of color from the solution). This indicates that in most cases, the actual amount of dye removed from the system through photodecolorization may be overestimated due to the contribution of adsorption. This also shows that photocatalysis is primarily a surface phenomenon. Second, with increase in calcination temperature of the TiO<sub>2</sub>-ZnO nanocomposite, the fraction of dye that remained adsorbed to the nanocomposite at the end of the study (240 min) decreased,

especially for the study employing visible light irradiation. Thus, the difference between the real and apparent values of dye decolorization may be expected to decrease with increase in calcination temperature, and hence, with increase in crystallinity. Two possible reasons were proposed to explain this phenomenon. As the rate of decolorization was enhanced at higher calcination temperatures (Fig. 7), the residual adsorption may have reduced due to decrease in the number of dye molecules in the system. Moreover, some by-products may have formed during the reaction and sorption of the by-products may have hindered sorption of the parent dye molecules. Further experiments are needed

to substantiate the above hypotheses. However, if it were true, it would indicate that with increased crystallinity, the efficiency of the nanocomposite to decolorize the parent compound increased, which in turn led to rapid decolorization and hence reduced residual sorption (Fig. 9). The reasons for the same may be many, such as increased surface area, decreased amorphousness and variation in porosity. These assumptions need further validation. Finally, and most importantly, in almost all cases, the % dye recovered by desorption was seen to be higher in case of TiO<sub>2</sub> nanoparticles, as opposed to the nanocomposites. This again suggests that while TiO<sub>2</sub> nanoparticles without ZnO showed % removal comparable to the nanocomposites, these were overestimated and in reality, even under UV irradiation, the nanocomposites showed better activity. Efficient charge separation due to incorporation of ZnO may be responsible for this phenomenon. The increased residual adsorption of dye by the TiO<sub>2</sub> nanoparticles under visible irradiation can be explained by their inferior activity under visible light. Therefore, while TiO<sub>2</sub> nanoparticles may have adsorptive capabilities comparable to their nanocomposite counterparts, the ability to produce electron–hole pairs (stemming from their inherent electronic properties such as bandgap) is poorer. Thus, the adsorbed molecules are unable to undergo degradation as effectively as in the nanocomposites.

## Conclusions

The TiO<sub>2</sub>–ZnO nanocomposite powder with an atomic molar ratio of Ti:Zn of 1:0.1 was produced through a sol–gel process. With increase in calcining temperature from 300 to 700 °C, the crystallinity of the composite powder was significantly improved. During this process, TiO<sub>2</sub> remained in its photocatalytically active anatase phase, except for particles calcined at 700 °C, which showed the initiation of phase transformation of anatase TiO<sub>2</sub> to rutile. The derived powder showed rough particle surfaces at lower calcination temperatures, which then evolved into equiaxed, almost cubical, smooth-surfaced particles with increase in calcination temperature. Bandgap of the nanocomposites was measured and it was observed that the addition of ZnO even at low molar concentration to the system enabled decrease in the bandgap, irrespective of the calcination temperature. The efficiency of the nanocomposites to utilize visible light was demonstrated by the photodecolorization of MO dye under UV and visible light sources. It was seen that, irrespective of the calcination temperature, the nanocomposites showed better visible light response as compared to their TiO<sub>2</sub> (without ZnO) counterparts. In addition, higher dye removal was obtained in particles calcined at higher temperatures, owing to increased crystallinity. An important finding was that in most cases, the photocatalytic activity of the catalysts may

be overestimated, since residual adsorption of the dye is rarely quantified at the end of the study. In the present study, it was found that while the TiO<sub>2</sub> nanoparticles (without ZnO) showed comparable or even slightly higher activity as compared to TiO<sub>2</sub>–ZnO nanocomposites under UV irradiation, this was an apparent value, and in absolute terms, the nanocomposites showed superior activity.

**Acknowledgements** The authors would like to extend their gratitude to the Sophisticated Analytical Instrument Facility (SAIF), IIT Bombay for FEG–SEM, EDAX, ICP–AES, and FTIR analyses, the Department of Chemistry for DRS measurements and the Department of Metallurgy Engineering and Materials Science (MEMS) for XRD analysis. Partial funding for this work was provided by the Department of Science and Technology, New Delhi, India under the Water Technology Initiative (WTI) scheme (Project code: DST/TM/WTI/2K15/101(G)).

## Compliance with ethical standards

**Conflict of interest** On behalf of all authors, the corresponding author states that there is no conflict of interest.

## References

- Al-Qaradawi S, Salman SR (2002) Photocatalytic degradation of methyl orange as a model compound. *J Photochem Photobiol A Chem* 148(1–3):161–168
- Araña J, Doña-Rodríguez JM, Portillo-Carrizo D, Fernández-Rodríguez C, Pérez-Peña J, Díaz OG, Navio JA, Macías M (2010) Photocatalytic degradation of phenolic compounds with new TiO<sub>2</sub> catalysts. *Appl Catal B* 100(1):346–354. <https://doi.org/10.1016/j.apcatb.2010.08.011>
- Athauda TJ, Neff JG, Sutherland L, Butt U, Ozer RR (2012) Systematic study of the structure–property relationships of branched hierarchical TiO<sub>2</sub>/ZnO nanostructures. *ACS Appl Mater Interfaces* 4(12):6917–6926. <https://doi.org/10.1021/am302061z>
- Bojinova A, Kralchevska R, Poulis I, Dushkin C (2007) Anatase/rutile TiO<sub>2</sub> composites: influence of the mixing ratio on the photocatalytic degradation of malachite green and orange II in slurry. *Mater Chem Phys* 106(2):187–192. <https://doi.org/10.1016/j.matchemphys.2007.05.035>
- Cai Y, Strømme M, Welch K, Cai YL (2014) Disinfection kinetics and contribution of reactive oxygen species when eliminating bacteria with TiO<sub>2</sub> Induced photocatalysis. *J Biomater Nanobiotechnol* 5(5):200–209. <https://doi.org/10.4236/jbnb.2014.53024>
- Cheng C, Amini A, Zhu C, Xu Z, Song H, Wang N (2014) Enhanced photocatalytic performance of TiO<sub>2</sub>–7ZnO hybrid nanostructures. *Sci rep* 4(4181):1–5. <https://doi.org/10.1038/srep04181>
- Choudhury B, Choudhury A (2013) Local structure modification and phase transformation of TiO<sub>2</sub> nanoparticles initiated by oxygen defects, grain size, and annealing temperature. *Int Nano Lett* 3(1):55. <https://doi.org/10.1186/2228-5326-3-55>
- Çomaklı O, Yazıcı M, Yetim T, Yetim AF, Çelik A (2016) The effect of calcination temperatures on structural and electrochemical properties of TiO<sub>2</sub> film deposited on commercial pure titanium. *Surf Coat Technol* 285:298–303. <https://doi.org/10.1016/j.surfcoat.2015.11.055>
- Conesa JJC (2012). Modeling with hybrid density functional theory the electronic band alignment at the zinc oxide–anatase interface. *J Phys Chem C*, 116(35): 18884–18890. <https://doi.org/10.1021/jp306160c>

- Das R, Sarkar S, Chakraborty S, Choi H, Bhattacharjee C (2014) Remediation of antiseptic components in wastewater by photocatalysis using TiO<sub>2</sub> nanoparticles. *Ind Eng Chem Res* 53(8):3012–3020. <https://doi.org/10.1021/ie403817z>
- De Angelis F, Di Valentin C, Fantacci S, Vittadini A, Selloni A (2014) Theoretical studies on anatase and less common TiO<sub>2</sub> phases: bulk, surfaces, and nanomaterials. *Chem Rev* 114(19):9708–9753. <https://doi.org/10.1021/cr500055q>
- Derikvandi H, Nezamzadeh-Ejhi A (2017) Increased photocatalytic activity of NiO and ZnO in photodegradation of a model drug aqueous solution: effect of coupling, supporting, particles size and calcination temperature. *J Hazard Mater* 321:629–638. <https://doi.org/10.1016/j.jhazmat.2016.09.056>
- Devi LG, Kavitha R (2013) A review on non metal ion doped titania for the photocatalytic degradation of organic pollutants under UV/solar light: role of photogenerated charge carrier dynamics in enhancing the activity. *Appl Catal B* 140:559–587. <https://doi.org/10.1016/j.apcatb.2013.04.035>
- Fox MA, Dulay MT (1993) Heterogeneous photocatalysis. *Chem rev* 93(1):341–357
- Gallardo JM, Vicente A, Escribano S, Buscab G (1995) Anatase crystal growth and phase transformation to Rutile in high- area TiO<sub>2</sub>, MOO<sub>3</sub>-TiO<sub>2</sub>, and other TiO<sub>2</sub>-supported oxide catalytic systems. *J Mater Chem*, 5(8):1245–1249. <http://pubs.rsc.org/en/content/articlepdf/1995/JM/JM9950501245>
- Gao J, Luan X, Wang J, Wang B, Li K, Li Y, Kang P, Han G (2011) Preparation of Er<sup>3+</sup>:YAlO<sub>3</sub>/Fe-doped TiO<sub>2</sub>-ZnO and its application in photocatalytic degradation of dyes under solar light irradiation. *Desalination* 268:68–75. <https://doi.org/10.1016/j.desal.2010.09.052>
- Gribb AA, Banfield JF (1997) Particle size effects on transformation kinetics and phase stability in nanocrystalline TiO<sub>2</sub>. *Am Mineral* 82(7–8):717–728. <https://doi.org/10.2138/am-1997-7-809>
- Janitabar-DarziAli S, Mahjoub R (2009) Investigation of phase transformations and photocatalytic properties of sol–gel prepared nanostructured ZnO/TiO<sub>2</sub> composites. *J Alloys Compd* 486(1–2):805–808. <https://doi.org/10.1016/J.JALLCOM.2009.07.071>
- Jing C, Rawson FJ, Zhou H, Shi X, Li WH, Li DW, Long YT (2014) New insights into electrocatalysis based on plasmon resonance for the real-time monitoring of catalytic events on single gold nanorods. *Anal Chem* 86(11):5513–5518. <https://doi.org/10.1021/ac500785u>
- Lei JF, Li LB, Shen XH, Du K, Ni J, Liu CJ, Li WS (2013) Fabrication of ordered ZnO/TiO<sub>2</sub> heterostructures via a templating technique. *Langmuir* 29(45):13975–13981
- Li G, Li L, Boerio-Goates J, Woodfield BF (2005) High purity anatase TiO<sub>2</sub> nanocrystals: near room-temperature synthesis, grain growth kinetics, and surface hydration chemistry. *J Am Chem Soc* 127(24):8659–8666. <https://doi.org/10.1021/ja050517g>
- Liang R, Hu A, Li W, Zhou YN (2013). Enhanced degradation of persistent pharmaceuticals found in wastewater treatment effluents using TiO<sub>2</sub> nanobelt photocatalysts. *J Nanoparticle Res*, 15(10):1990. <https://doi.org/10.1007/s11051-013-1990-x>
- Liao DL, Badour CA, Liao BQ (2008) Preparation of nanosized TiO<sub>2</sub>/ZnO composite catalyst and its photocatalytic activity for degradation of methyl orange. *J Photochem Photobiol A* 194(1):11–19. <https://doi.org/10.1016/j.jphotochem.2007.07.008>
- Little ME, Kordesch ME (2001) Band-gap engineering in sputter-deposited Sc<sub>x</sub>Ga<sub>1-x</sub>N. *Appl Phys Lett* 78(19):2891–2892. <https://doi.org/10.1063/I.1370548>
- Luttrel T, Halpegamage S, Tao J, Kramer A, Sutter E, Batzill M (2014) Why is anatase a better photocatalyst than rutile? Model studies on epitaxial TiO<sub>2</sub> films. *Sci Rep* 4:4043. <https://doi.org/10.1038/srep04043>
- Méndez-Arriaga F, Esplugas S, Giménez J (2008) Photocatalytic degradation of non-steroidal anti-inflammatory drugs with TiO<sub>2</sub> and simulated solar irradiation. *Water Res* 42:585–594. <https://doi.org/10.1016/j.watres.2007.08.002>
- Minero C, Catozzo F, Pelizzetti E (1992). Role of adsorption in photocatalyzed reactions of organic molecules in aqueous TiO<sub>2</sub> suspensions. *Langmuir* 8:481–486. <https://doi.org/10.1021/la00038a029>
- Mo SD, Ching WY (1995) Electronic and optical properties of three phases of titanium dioxide: rutile, anatase, and brookite. *Phys Rev B* 51(19):13023–13032. <https://doi.org/10.1103/PhysRevB.51.13023>
- Mozaffari S, Li W, Thompson C, Ivanov S, Seifert S, Lee B, Koverick L, Karim AM (2017) Colloidal nanoparticle size control: experimental and kinetic modeling investigation of the ligand–metal binding role in controlling the nucleation and growth kinetics. *Nanoscale* 9(36):13772–13785
- Nguyen NC, Lin BL, Chen SS (2013) A novel treatment method for acetaminophen in pharmaceutical wastewater by photocatalysis with various electron accepters. *J Eng Technol Educ* 9(5):8–14
- Nishio J, Tokumura M, Znad HT, Kawase Y (2006) Photocatalytic decolorization of azo-dye with zinc oxide powder in an external UV light irradiation slurry photoreactor. *J Hazard Mater* 138(1):106–115. <https://doi.org/10.1016/j.jhazmat.2006.05.039>
- Odling G, Robertson N (2015) Why is anatase a better photocatalyst than rutile? The importance of free hydroxyl radicals. *Chem Sus Chem* 8(11):1838–1840. <https://doi.org/10.1002/cssc.201500298>
- Pei CC, Leung WWF (2013) Photocatalytic degradation of rhodamine B by TiO<sub>2</sub>/ZnO nanofibers under visible-light irradiation. *Sep Purif Technol* 114:108–116. <https://doi.org/10.1016/j.seppur.2013.04.032>
- Pelaez M, Nolan NT, Pillai SC, Seery MK, Falaras P, Kontos AG, Dunlop PSM, Hamilton JWW, Byrne JA, O’Shea K, Entezari MH (2012) A review on the visible light active titanium dioxide photocatalysts for environmental applications. *Appl Catal B* 125:331–349. <https://doi.org/10.1016/j.apcatb.2012.05.036>
- Rajbongshi BM, Samdarshi SK, Boro B (2015) Multiphasic bi-component TiO<sub>2</sub>-ZnO nanocomposite: synthesis, characterization and investigation of photocatalytic activity under different wavelengths of light irradiation. *J Mater Sci Mater Electron* 26(1):377–384. <https://doi.org/10.1007/s10854-014-2410-4>
- Rizzo L, Meric S, Guida M, Kassinos D, Belgioirno V (2009) Heterogeneous photocatalytic degradation kinetics and detoxification of an urban wastewater treatment plant effluent contaminated with pharmaceuticals. *Water Res* 43:4070–4078. <https://doi.org/10.1016/j.watres.2009.06.046>
- Rodríguez-Méndez A, Guzmán C, Elizalde-Peña EA, Escobar-Alarcón L, Vega M, Rivera JA, Esquivel K (2017) Effluent disinfection of real wastewater by Ag-TiO<sub>2</sub> nanoparticles photocatalysis. *J Nanosci Nanotechnol* 17(1):711–719. <https://doi.org/10.1166/jnn.2017.13066>
- Schneider J, Matsuoka M, Takeuchi M, Zhang J, Horiuchi Y, Anpo M, Bahnemann DW (2014) Understanding TiO<sub>2</sub> photocatalysis: mechanisms and materials. *Chem Rev* 114:9919–9986. <https://doi.org/10.1021/cr500189z>
- Shahram M, Aberoomand-Azar P, Raeis-Farshid S, Abedini-Khorrami S, Hadi Givianrad M (2016) The effect of different molar ratios of ZnO on characterization and photocatalytic activity of TiO<sub>2</sub>/ZnO nanocomposite. *J Saudi Chem Soc* 20(4):373–378. <https://doi.org/10.1016/J.JSCS.2012.08.002>
- Spurr RA, Myers H (1957). Quantitative analysis of anatase-rutile mixtures with an X-ray diffractometer. *Anal Chem*, 29(5): 760–762. <https://doi.org/10.1021/ac60125a006>
- Su W, Zhang J, Feng Z, Chen T, Ying P, Li C (2008) Surface phases of TiO<sub>2</sub> nanoparticles studied by UV Raman spectroscopy and FT-IR spectroscopy. *J Phys ChemC* 112(20):7710–7716. <https://doi.org/10.1021/jp711842z>
- Tsuang YH, Sun JS, Huang YC, Lu CH, Chang WHS, Wang CC (2008) Studies of photokilling of bacteria using titanium dioxide

- nanoparticles. *Int J Artif Organs* 32(2):167–174. <https://doi.org/10.1111/j.1525-1594.2007.00530.x>
- Wang J, Mi W, Tian J, Dai J, Wang X, Liu X (2013) Effect of calcinations of TiO<sub>2</sub>/ZnO composite powder at high temperature on photodegradation of methyl orange. *Compos Part B* 45(1):758–767. <https://doi.org/10.1016/j.compositesb.2012.09.053>
- Yakuphanoglu F, Ilican S, Caglar M, Caglar Y (2007) The determination of the optical band and optical constants of non-crystalline and crystalline ZnO thin films deposited by spray pyrolysis. *J Optoelectron Adv Mater* 9(7):2180–2185
- Yu J, Wang B (2010). Effect of calcination temperature on morphology and photoelectrochemical properties of anodized titanium dioxide nanotube arrays. *Appl Catal B*, 94(3): 295–302. <https://doi.org/10.1016/j.apcatb.2009.12.003>
- Zhang Q, Gao L, Guo J (2000) Effects of calcination on the photocatalytic properties of nanosized TiO<sub>2</sub> powders prepared by TiCl<sub>4</sub> hydrolysis. *Appl Catal B* 26:207–215. [https://doi.org/10.1016/S0926-3373\(00\)00122-3](https://doi.org/10.1016/S0926-3373(00)00122-3)
- Zhang J, Zhou P, Liu J, Yu J (2014) New understanding of the difference of photocatalytic activity among anatase, rutile and brookite TiO<sub>2</sub>. *Phys Chem* 16(16):20382–20386. <https://doi.org/10.1039/c4cp02201g>

**Publisher's Note** Springer Nature remains neutral with regard to jurisdictional claims in published maps and institutional affiliations.